Nuclear Science and Techniques (2023) 34:76
https://doi.org/10.1007/s41365-023-01227-x

Resolution analysis of thermal neutron radiography based on accelerator-driven compact neutron source

Lian-Xin Zhang[1,2] · Si-Ze Chen[1,2] · Zao-Di Zhang[1] · Tao-Sheng Li[1,2] · Chuan Peng[1,2] · Lei Ren[1,2] · Rui Zhang[1,2] · Dan Xiao[1] · Yong Zhang[1]

Received: 20 October 2022 / Revised: 27 February 2023 / Accepted: 28 February 2023 / Published online: 26 May 2023

Abstract
Owing to the immobility of traditional reactors and spallation neutron sources, the demand for compact thermal neutron radiography (CTNR) based on accelerator neutron sources has rapidly increased in industrial applications. Recently, thermal neutron radiography experiments based on a D-T neutron generator performed by Hefei Institutes of Physical Science indicated a significant resolution deviation between the experimental results and the values calculated using the traditional resolution model. The experimental result was up to 23% lower than the calculated result, which hinders the achievement of the design goal of a compact neutron radiography system. A GEANT4 Monte Carlo code was developed to simulate the CTNR process, aiming to identify the key factors leading to resolution deviation. The effects of a low collimation ratio and high-energy neutrons were analyzed based on the neutron beam environment of the CTNR system. The results showed that the deviation was primarily caused by geometric distortion at low collimation ratios and radiation noise induced by high-energy neutrons. Additionally, the theoretical model was modified by considering the imaging position and radiation noise factors. The modified theoretical model was in good agreement with the experimental results, and the maximum deviation was reduced to 4.22%. This can be useful for the high-precision design of CTNR systems.

Keywords Neutron radiography · Spatial resolution · Accelerator-driven neutron source · Geant4 · MTF · ESF

1 Introduction

Neutron radiography has been established as an important non-destructive inspection method and quantitative measurement tool [1]. Because thermal neutrons can provide a strong contrast for some elements close to one another in the periodic table and can even distinguish isotopes of the same element, neutron radiography can provide complementary X-ray and gamma-ray radiography [2]. It is widely used in the aerospace industry, national defense, materials energy, biological archeology, and other fields. Currently, thermal neutron radiography (TNR) is an important field in the development of neutron radiography [3]. However, the traditional TNR is mainly based on an expensive, bulky, and immovable reactor or spallation neutron source, which greatly limits its application. Compact thermal neutron radiography (CTNR) can mitigate these challenges [4, 5].

In contrast to conventional TNR, CTNR commonly uses a compact accelerator as the neutron generator. Accelerator-driven neutron sources (such as D-D or D-T neutron generators) require complex moderator and collimator configurations to create neutron beams with suitable radiographic properties [6]. Its intensity is 2–3 orders of magnitude lower than that of the reactor or spallation neutron source. Consequently, the quality of the available neutron beam after moderation and collimation is significantly lower than that of conventional neutron radiography, which mainly manifests as a low collimation ratio (L/D) (Table 1) and low thermal neutron content (Fig. 1) [5, 7]. Both of these factors have an adverse effect on imaging resolution, but are less considered

This work was supported by the Nuclear Energy Development Project of China (No. [2019]1342) and the Presidential Foundation of HFIPS (No. YZJJ2022QN40).

✉ Si-Ze Chen
size.chen@inest.cas.cn

[1] Hefei Institutes of Physical Science, Chinese Academy of Sciences, Hefei 230031, China

[2] University of Science and Technology of China, Hefei 230026, China

Table 1 Parameters of TNR facility

Type	Neutron source	Imaging neutron flux (n/s/cm^2)	*L*/*D*	Imaging area (cm^2)	Spatial resolution (μm)
Reactor	IBR-2 [8]	~5.52×10^6	200–2000	20×20	300
Reactor	WWR-K [9]	~7.1×10^6	75–1400	20×20	232.2
Reactor	PULSTAR [10]	1.8×10^6–7×10^6	100–150	2.7×2.7	84
Spallation	RANS [11]	~10^4	21–781	17×17	40
Accelerator	BARC [12]	~4×10^3	20	20×20	~1000
Accelerator	PKUNIFTY [13]	2.35×10^4	50–200	21×21	330
Accelerator	CAEP [14]	~1×10^4	~25	20×20	500
Accelerator	INEST	~1×10^4	~15	20×20	600

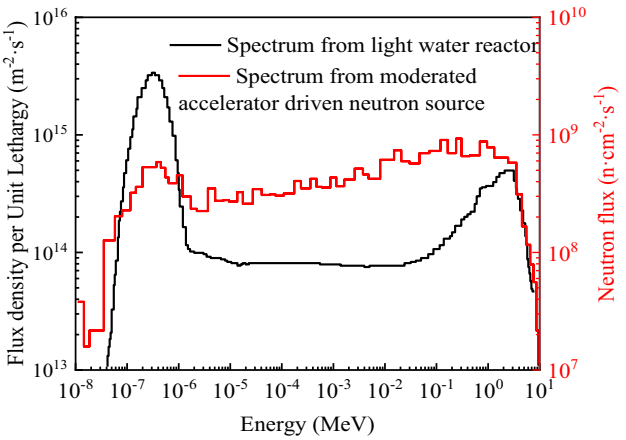

Fig. 1 (Color online) Comparison of neutron spectrum between the reactor and moderator

for conventional TNR systems. Based on this background, this paper presents an in-depth study of the resolution of a CTNR system.

2 Shortcoming of the traditional theoretical resolution model

2.1 The traditional resolution model of neutron radiography

The modular transfer function (MTF) is a classical resolution analysis method based on the frequency domain derived from the Fourier transform of a point spread function (PSF). Compared with the PSF and other spatial domain methods, the MTF method has higher accuracy in resolution calculation. The MTF is defined as the ratio of the output modulation to the input modulation. The MTF of an image can be calculated using the following equation [15]:

$$\mathrm{MTF}(f)=\frac{M_{\mathrm{out}}}{M_{\mathrm{in}}}=\frac{(I'_{\max}-I'_{\min})/(I'_{\max}+I'_{\min})}{(I_{\max}-I_{\min})/(I_{\max}+I_{\min})} \tag{1}$$

where $I'_{\max}$ is the maximum gray value at the target area of the output image, $I'_{\min}$ is the minimum gray value of the output image, $I_{\max}$ is the maximum gray value of the target area of the input image, and $I_{\min}$ is the minimum gray value of the input image. According to the Rayleigh criterion, the spatial resolution of an image is defined as the corresponding resolution of the 10% MTF [16]. Furthermore, the MTF method can be used to analyze the effects of system elements on the spatial resolution.

The model of resolution is essential for designing a TNR system to ensure that realistic resolution goals are established and achieved. The traditional theoretical resolution model focuses on the TNR system structure, which comprises a collimator, converter screen, and imaging system [15]. Assuming that the effects of these components on the imaging resolution are independent of each other, the total MTF of a digital thermal neutron imaging system can be analytically produced through a Fourier transformation [17]:

$$\mathrm{MTF}(u)=\sin c\left(\frac{d}{\frac{L}{D}}u\right)\cdot\exp\left(-\pi(\delta u)^2\right)\cdot\sin c\left(\frac{\Delta s}{M_{\mathrm{CCD}}}u\right), \tag{2}$$

where u is the spatial frequency of imaging, d is the distance of the converter screen from the sample, D is the diameter of the neutron aperture, L is the distance from the aperture to the sample, δ is the optical diffusion response of the converter screen, Δs is the sampling at the sensor, M_{CCD} is the scintillator-to-CCD magnification, and $\Delta s/M_{\mathrm{CCD}}$ is image sampling on the converter screen. The MTF describes the magnitude of the system's frequency response. The theoretical resolution model is helpful for depicting and quantifying the system resolution.

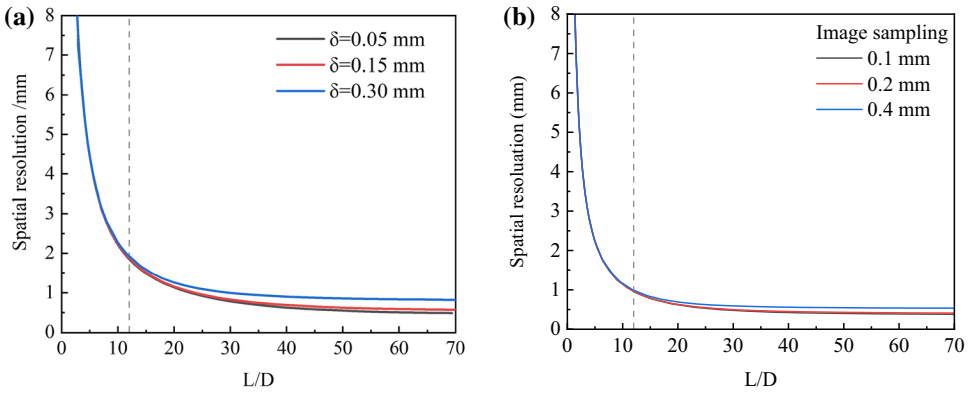

Fig. 2 (Color online) Relationship between resolution and *L*/*D*: **a** optical diffusion response and **b** image sampling

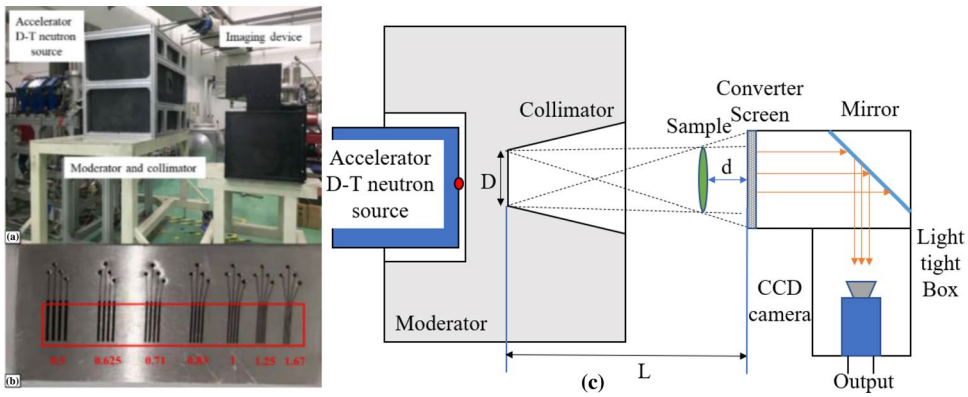

Fig. 3 (Color online) Experimental setup for the HFIPS: **a** picture of the terminal, **b** picture of the line-pair sample, and **c** schematic of the setup

2.2 The deviation of the theoretical resolution model applied to CTNR

Based on the traditional theoretical resolution model, this study analyzed the factors affecting the imaging resolution of a TNR system driven by the typical accelerator neutron source listed in Table 1. Figure 2 shows the relationship between the resolution and *L*/*D* with different optical diffusion responses and image samplings on the converter screen. When the *L*/*D* ratio is less than 12, the curves for each parameter coincide. This result indicates that the influence of the converter screen and image sampling is small in the resolution analysis at a low *L*/*D* ratio and that the *L*/*D* ratio becomes the most important factor affecting the resolution.

To verify the applicability of the theoretical model, a standard line-pair (Fig. 3b) sample neutron radiography experiment was performed based on the TNR terminal with a *D*-*T* fusion neutron source (Fig. 3a) built by Hefei Institutes of Physical Science (HFIPS), Chinese Academy of Sciences. The iron sample had dimensions of 50 mm × 100 mm × 10 mm and seven line pairs of 0.5, 0.62, 0.83, 1.0, 1.67, and 2.0 lp/mm separately. A schematic of the system is shown in Fig. 3c. Table 2 lists the characteristics of the neutron beam emitted by the moderated collimator of the neutron radiography terminal and the information of the imaging system.

Table 2 Parameters of compact thermal neutron radiography facility in INEST

Parameter	Value
Thermal neutron flux (n/cm^2/s)	1.5×10^3 to 2×10^4
L/*D*	7.5 to 15
Divergence (°)	~8.5
Field of view (FOV) (cm^2)	20 × 20
Converter screen	^{6}LiF/ZnS (Ag) 1:2
Pixel number (pixel)	1024 × 1024
Pixel size (μm^2)	13 × 13

Neutron radiography experiments were conducted using *L*/*D* values of 6.3, 7.4, 8.8, 10, and 12, respectively. The imaging exposure time was 300 s. Figure 4 shows the radiography results of line pairs with different *L*/*D* ratios. The center of the imaging field of view (FOV) coincided with the center of the neutron beam. Figure 4a shows the neutron radiograph with *L*/*D* = 7.4. The red box in the figure represents the sampling area of the line-pair image, and the corresponding gray curve was obtained. The gray curves of the images with other *L*/*D* ratios are shown in Fig. 4b.

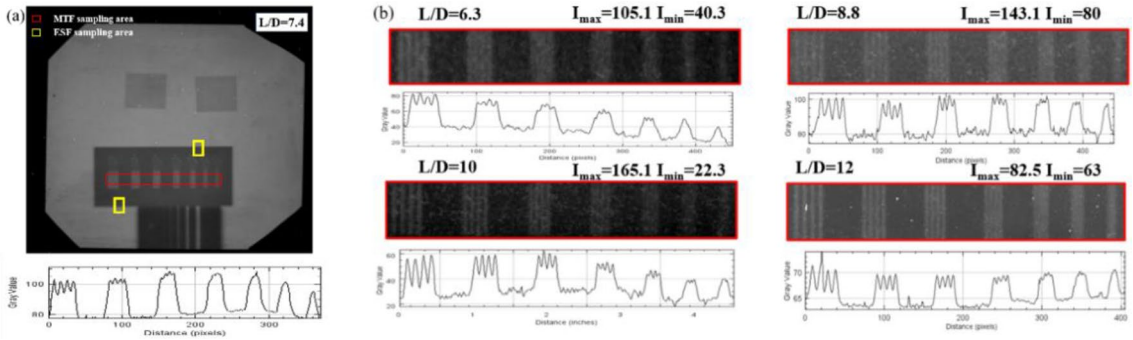

Fig. 4 (Color online) Results of the standard line-pair sample experiment: **a** result with $L/D = 7.4$ and corresponding sampling area; **b** results with other L/D ratios

The corresponding MTF(f) function value of each line-pair image can be obtained by substituting the gray value into Eq. (1). Then, the image resolution was obtained according to MTF = 0.1 by using the interpolation method, as shown in Fig. 5a. The theoretical resolution results under the same conditions were calculated using Eq. (2). A comparison between the experimental results and the theoretical resolution curve is shown in Fig. 5b. The results show that the image resolution improves with an increase in L/D in both the experimental data and theoretical calculations. However, all the experimental points were higher than the theoretical calculation curve, and the maximum deviation reached 23.1%. There was a significant deviation between the theoretical model and the experimental results, and the reason for this deserves further study.

3 Analysis of main parameters affecting spatial resolution and resolution deviation

In this section, the effects of a low L/D ratio and a high proportion of nonthermal neutrons on the imaging resolution are discussed to elucidate the reasons for the deviation mentioned above based on the Monte Carlo simulation numerical analysis method, which is performed on the GEANT4 framework [18]. The G4TENDL database [19], which has been proven to have high computational accuracy in previous studies [20], was used in the Monte Carlo calculations.

3.1 Effect of low L/D ratio on CTNR system

3.1.1 Geometric distortion

In this study, a GEANT4 Monte Carlo calculation model was built based on a theoretical resolution model. As shown in Fig. 6, the model consisted of three modules: a surface neutron source with a diameter of 9 cm, a converter screen with an area of 20 cm × 20 cm, and a position-sensitive detector. The surface neutron source was used to replace the accelerator neutron source and moderator to simulate the neutron beams emitted from an ideal neutron aperture. The converter screen material was ^{6}LiF/ZnS and its specific parameters are listed in Table 3 [21]. The photon-emission spectra of the converter screen and other scintillation parameters were set according to previous studies [22]. The position-sensitive detector was affixed to the back of the converter screen. The single pixel sampling area of the detector is 0.2 mm × 0.2 mm, which is consistent with the projection of CCD camera pixels on the converter screen. This detector

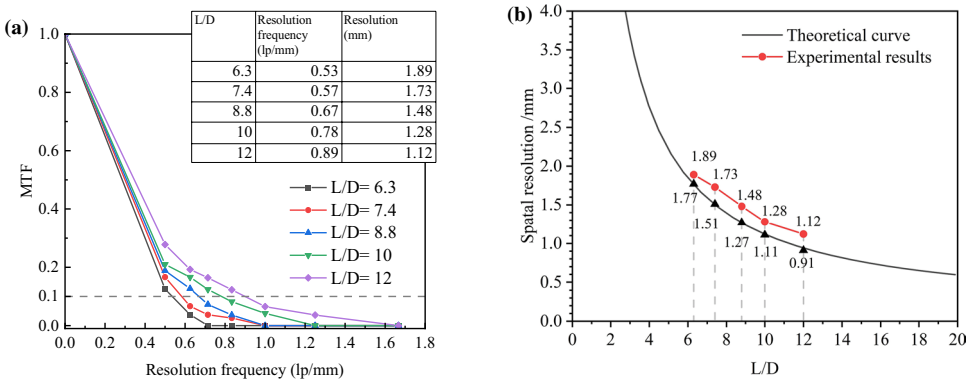

Fig. 5 (Color online) MTF Calculation results: **a** under different L/D conditions and **b** comparison between experimental results and theoretical curves

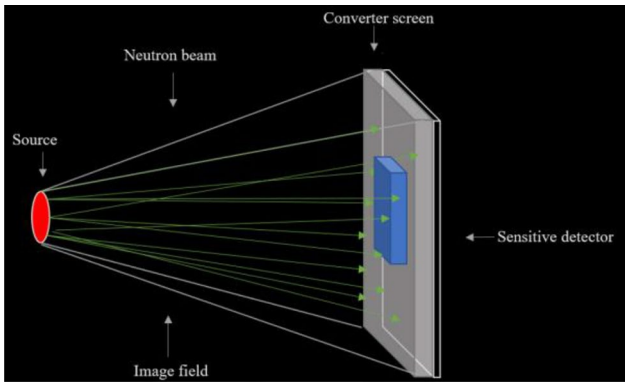

Fig. 6 (Color online) Model of the ideal TNR system used in the GEANT4 simulation program

Table 3 Optical properties of the converter screen [21, 22]

Properties	Specification
Material	^{6}LiF/ZnS 1:2
Dopant	Ag
Density (g/cm^3)	2.6
Optical photon yield/neutron	160,000
Decay time (μs)	1
Converter screen thickness (μm)	400

is used to record information about the number and position of photons produced from the converter screen [23], which generates grayscale images for comparison with the experimental results. Based on this model, the effect of neutron beam characteristics on resolution can be analyzed using an arbitrary *L*/*D* parameter.

The edge-spread function (ESF) method was used to extract the resolutions at different locations in the simulated image [24]. In this method, an opaque sample with a straight edge is used as the image object, and the curve of the gray-level change in the direction of the vertical image edge in the image plane is called the ESF curve. The spatial resolution was defined as the distance between 10 and 90% of the ESF curve [25]. A schematic of the resolution measurement simulation model using the ESF method is shown in Fig. 7. The red box in the figure represents the imaging sampling area, and the center of the red box is located on the edge of the sample. The relative distance between the edge of the sample and the imaging center was defined as d_c. The sample used in the experiment was a 1 cm-thick rectangular iron block. Different images were obtained in the simulations by adjusting the edge positions of the samples. The curves of the gray values of the images were obtained from the simulation images, and the resolution of each position was calculated using the ESF method.

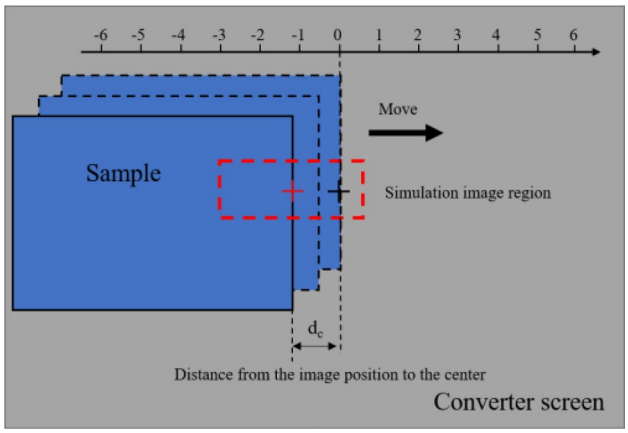

Fig. 7 (Color online) Schematic of the resolution of each position measured using the ESF method

The simulation results were compared with experimental images to verify the accuracy of the simulation. The yellow boxes shown in Fig. 4 ($L/D = 7.4$) are selected as the sampling areas with $d_c = 1.0$ cm and $d_c = 5.0$ cm. The gray images extracted from the experimental image are presented together with the images obtained from the simulations with the same parameters of d_c in Fig. 8a. The gray curves extracted from these images are compared in Fig. 8b. The results show that the simulated curves agree well with the experimental curves. The calculated resolution of the simulated image deviated from the experimental data by less than 4.5%.

Based on the validated simulation analysis method, the imaging resolutions with $L/D = 7.4$ at different positions were first calculated. The simulation results are shown in Fig. 9a. The black line represents the spatial resolutions at different positions, as shown in Fig. 7, and the red line represents the deviations between the simulated and theoretical resolutions. In Fig. 9a, the resolution curve exhibits a symmetrical structure, and the deviations increase linearly with d_c. To further study the influence of d_c on the resolution under different *L*/*D* conditions, images with five different *L*/*D* ratios were simulated, and resolutions at different imaging positions were obtained. Figure 9b presents the variations in the deviations between the simulation and theoretical calculation results at different d_c positions. The results show an incremental deviation as d_c increases, which gradually narrows as *L*/*D* increases. Another interesting result (Fig. 9b) is that the simulation results are consistent with the resolutions of the theoretical model at the center of the image ($d_c = 0$), and the maximum deviation is less than 2.7%.

The experimental data analysis provided a result similar to that of the Monte Carlo simulation. Figure 9c presents the ESF curves derived from the experimental data for $L/D = 7.4$ and $L/D = 12$. Under different *L*/*D* conditions,

there was a significant deviation between the imaging locations $d_c = 1$ cm and $d_c = 5$ cm. Moreover, the deviation with a smaller *L*/*D* ratio is larger. The experimental data intuitively show the impact of geometric distortion on the imaging resolution.

Based on the above analysis, it can be concluded that geometric distortion is an important factor that leads to resolution deterioration. Under low collimation conditions, the resolution deterioration caused by geometric distortion increases linearly with d_c.

To explore the mechanism underlying this phenomenon, the neutron beam emission angle distribution was calculated using a previously built Monte Carlo simulation model. Neutron emission angles were recorded on the front surface of the converter screen at different d_c intervals. Figure 10a presents the calculation results with the d_c value intervals of 0–1 cm, 1–2 cm, 3–4 cm, 5–6 cm, 7–8 cm, and 9–10 cm under the condition of $L/D = 10$; Fig. 10b presents the calculation results of the d_c value range of 4.5–5.5 with 5 different *L*/*D* ratios.

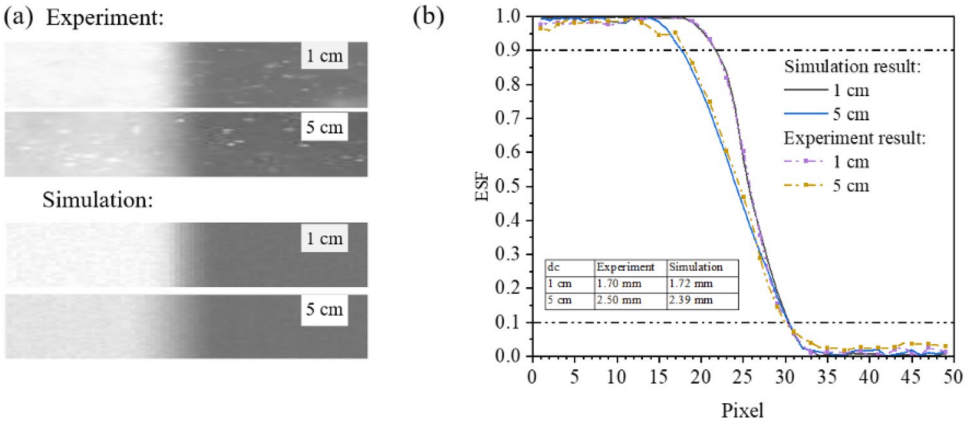

Fig. 8 (Color online) Comparison of experimental and simulation results: **a** gray image of sample edge and **b** corresponding gray curve

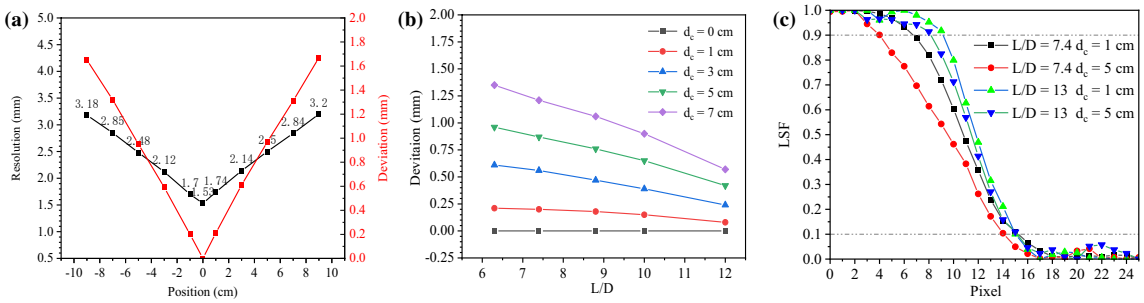

Fig. 9 (Color online) Resolution analysis of geometric distortion by LSF method: **a** simulation results of relationship between resolution and d_c with $L/D = 7.4$, **b** variation of deviations between simulation results and theoretical calculation results with different *L*/*D* ratios, and **c** experimental ESF curve comparison of line-pair edge images with different *L*/*D* ratios

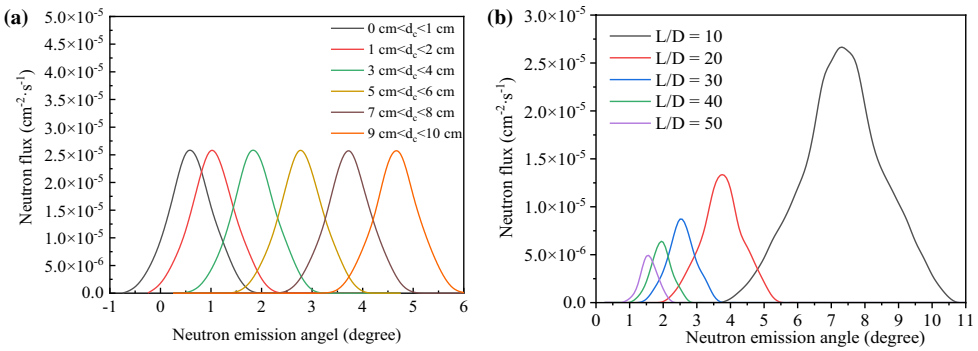

Fig. 10 (Color online) Results of neutron angle distribution with different **a** d_c values and **b** *L*/*D* values

The results in Fig. 10 show that when only d_c increased, the Gaussian widths of the neutron emission angle did not change significantly, whereas the average neutron emission angle gradually increased. When d_c is fixed, the average values of neutron emission angle decrease with L/D. These results indicate that the degradation of the image resolution is related to the average value of the neutron emission angle, which can be derived from the parameter d_c.

Based on the above considerations, a theoretical derivation was performed in this study. Figure 11 shows the geometric layout of the collimator, object, and converter screen. The offset distance d_g between the original and actual positions can be calculated based on a simple trigonometric relation:

$$d_g = \frac{d_c \cdot d}{L}, \tag{3}$$

where d_c is the distance from the object to the imaging center, L is the distance from the aperture to the object, and d is the distance from the object to the screen.

An oblique-incidence neutron beam also results in geometric distortion on the converter screen. A schematic of the NIL process on the converter screen is shown in Fig. 12. The offset distance can be calculated using Eq. (4) as follows:

$$d_s = \frac{d_c \cdot t}{L} \tag{4}$$

where d_s is the offset of the light output on the converter; t is the thickness of the converter screen as the effective photon yield is generated mainly by neutrons that react at the bottom of the screen; and L is the distance from the collimator aperture to the converter screen. The offset is proportional to t and d_c and inversely proportional to the L/D ratio. Figure 13 shows the simulation results of the light spot generated by a neutron beam with different d_c under the $L/D = 10$ condition.

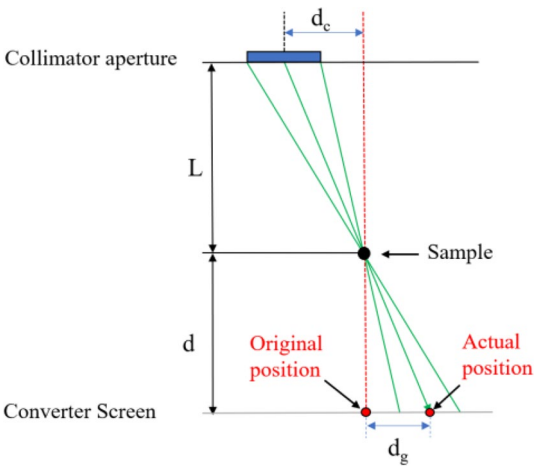

Fig. 11 Schematic of geometrical distortion in neutron radiography

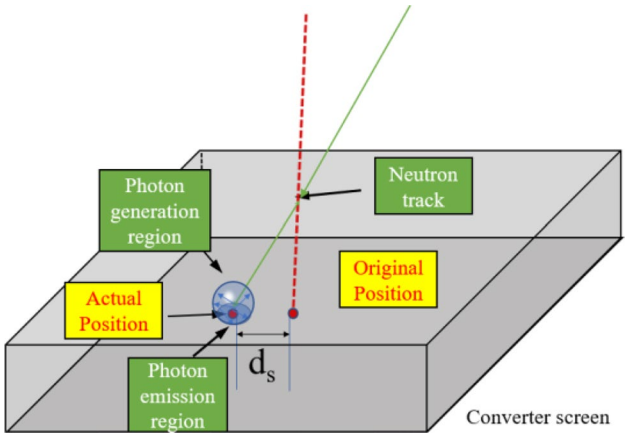

Fig. 12 (Color online) Schematic of geometrical distortion on the converter screen

A phenomenon in which d_s moves proportionally with d_c can be observed.

Both offsets introduced before blurred the image of the object edge and deteriorated the resolution. Geometric distortion is caused by the physical characteristics of the beam emission angle. This can also be observed in the traditional TNR and other optical imaging systems [26]. In contrast to the CTNR system, L/D is usually very large in these imaging areas, and the effect of geometric distortion is usually insignificant.

3.1.2 Effect on converter screen characteristics

The characteristic parameters of a converter screen include the photon yield and optical diffusion response [27]. A series of calculations was performed to study the characteristics of the converter screen. In the neutron radiography system, the optical diffusion response (δ) of the converter screen can be calculated as follows [16]:

$$h_s(x, y) = \exp\left[-\pi \frac{x^2 + y^2}{\delta^2}\right], \tag{5}$$

where $h_s(x, y)$ is the light output distribution induced by a single neutron beam from the converter screen. Figure 14a shows the Monte Carlo simulation results of the photon output behind the converter screen, which conform to the Gaussian distribution of Eq. (5). The Gaussian widths of the photon distribution with a large L/D ratio were obviously smaller than those with a small L/D ratio, whereas the neutron light yield in the spot center decreased with the deterioration of L/D. Figure 14b compares δ fitting from Fig. 14a and the total neutron light yield together. δ of the converter screen shows a negative relationship with the L/D ratio, which is consistent with the analysis results presented

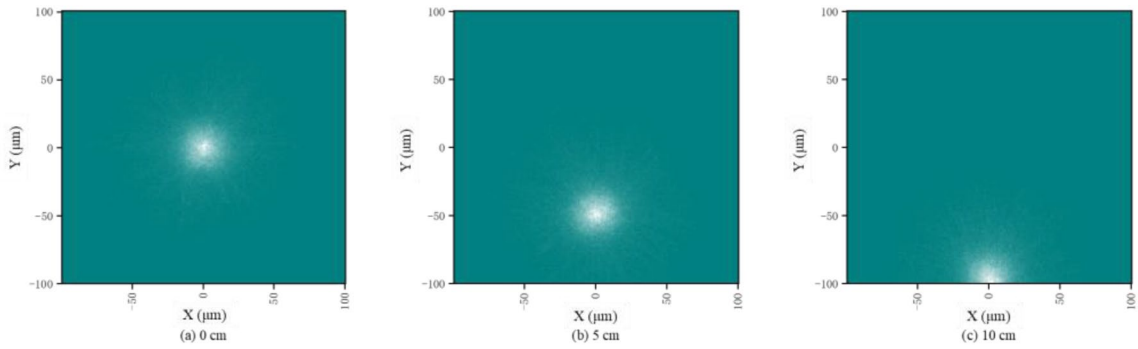

Fig. 13 (Color online) Light spots generated by the neutron beam vary with $d_c = 0$ cm **a**, $d_c = 5$ cm **b**, and $d_c = 10$ cm **c**.

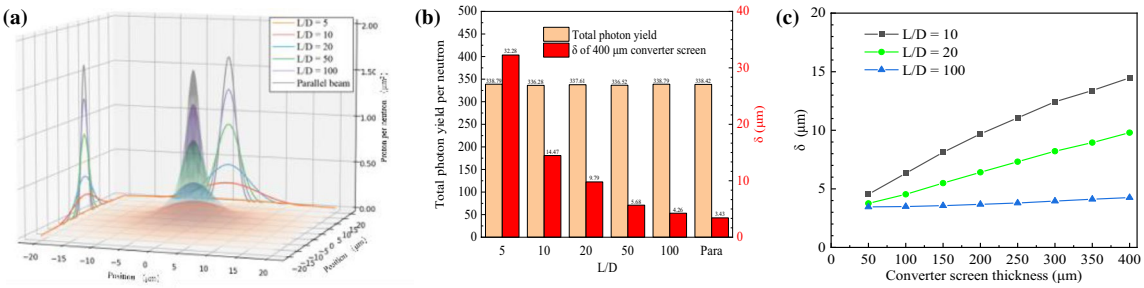

Fig. 14 (Color online) Different characteristics of converter screen: **a** photon output distribution with different *L/D* ratios, **b** comparison between photon yield and δ with different *L/D* ratios, and **c** relationship between δ and the thickness of converter screen

in Fig. 14a. However, under different *L/D* conditions, the total photon yield of the neutrons was approximately the same. This indicates that the *L/D* ratio did not affect the light output of the converter screen. Figure 14c shows the variation curve of the optical diffusion response versus screen thickness under different *L/D* conditions. When $L/D = 100$, the curve shows few correlations; however, the other two curves exhibit evident positive correlations. In addition, the effect of conversion screen thickness on δ increases significantly with the decrease in collimation ratio.

In an ideal neutron radiography model, different components are considered independent of each other. However, from the analyses above, we can find that under a low *L/D* condition, a change in *L/D* ratio will affect δ of the converter screen. This is one of the factors potentially leading to the deterioration of the resolution observed in the experiments. When the thickness of the converter screen is set to 100 μm as used in the experiment, δ is 6.32 μm with $L/D = 10$ and 3.49 μm with $L/D = 100$. In this situation, the MTF change caused by δ is only 0.89% on the limiting resolution of devices (1 lp/mm). This result shows that the change of δ under different *L/D* conditions can affect the image resolution. However, the effect of δ is not obvious.

3.2 Effect of high-energy neutrons on CTNR system

3.2.1 Effect on converter screen

In the CTNR system, a moderator is used to moderate fast neutrons from the accelerator. To study the relationship between the neutron energy and spatial resolution, a CTNR system model is proposed, as shown in Fig. 15a. An 8 cm-thick lead layer was used as the first layer of the moderator and a 5 cm-thick polyethylene layer was used as the second layer to obtain thermal neutrons. The reflective layer material was 15 cm-thick graphite. This design can significantly improve the thermal neutron flux [28, 29]. Before the first layer of moderator, a 14 MeV surface neutron source with a diameter of 1 cm was set on the central axis of the moderator to simulate accelerator neutron source beam spot. This model was used to study the thermal neutron flux, neutron beam energy spectrum, and photon yield in a CTNR system. Figure 15b presents the energy spectrum of the neutron beam emitted from the moderator. The proportion of thermal neutrons in the neutron beam was only 9.13%, which indicated that numerous nonthermal neutrons still existed in the moderated neutron beam. Therefore, it is necessary to study the effects of nonthermal neutrons on imaging.

Nonthermal neutrons work with the converter screen through different cross sections. Therefore, the photon yield with neutrons of different energies was first calculated (Fig. 16a). The photon yield was roughly consistent with the microscopic cross section of ^{6}Li. Figure 16b shows the simulation results of the photon yield produced by the neutron beam exiting the moderator. The proportion of photons generated by thermal neutrons was 95.79%, whereas that of photons generated by nonthermal neutrons was 4.21%. Based on the above results, the effect of nonthermal neutrons on the imaging resolution can be neglected in CTNR systems, even with a low proportion of thermal neutron beams.

3.2.2 Effect on CCD

The shielding of a CTNR system is limited by its geometric dimensions, and it is difficult to completely shield high-energy neutrons and their secondary gamma rays. When radiation particles reach the CCD chip, they deposit energy that generates electronic noises [30]. The noisy images obtained under different experimental conditions are shown in Fig. 17. As shown in the figure, the effect of white spot noise cannot be neglected, even with shielding. The proportions of noise in the neutron radiography images with and without shielding were 2.07% and 7.09%, respectively.

The presence of radiation noise in images is harmful to the quantitative analysis of the resolution. The ESF and MTF methods are based on the numerical analysis of the

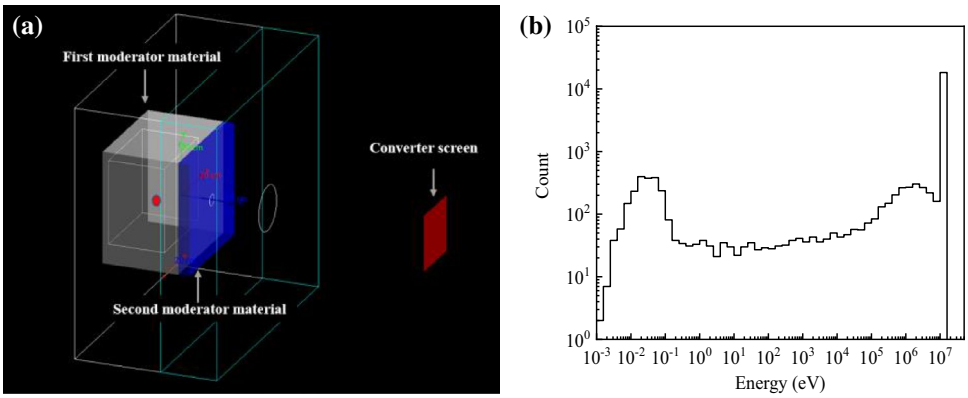

Fig. 15 (Color online) Simulation of the CTNR system: **a** GEANT4 model and **b** neutron energy spectrum on the converter screen

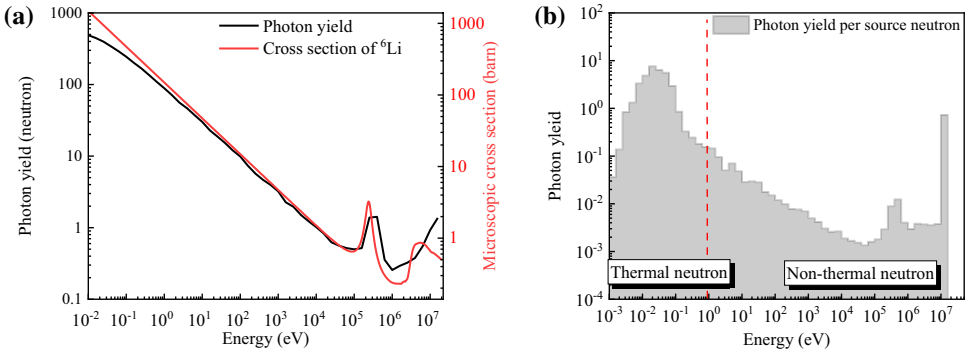

Fig. 16 (Color online) Simulation results of photon yield: **a** photon yield of different energy neutrons and **b** light yield distribution of neutrons exiting the moderator

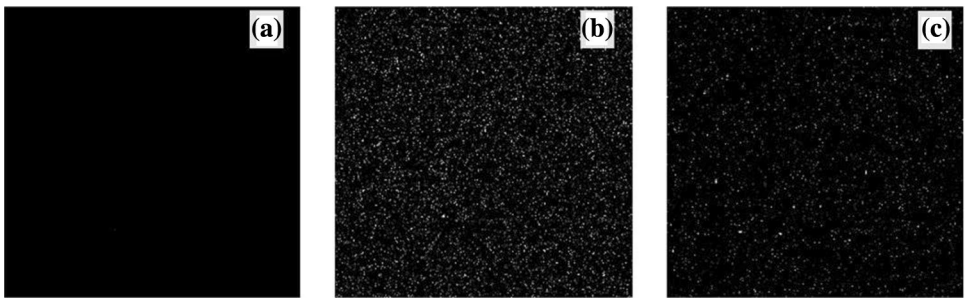

Fig. 17 Noisy images under different experimental conditions: **a** before the experiment, **b** without shielding, and **c** with shielding

Table 4 Comparison of resolutions obtained by different methods

d_c (cm)	Experiment	Simulation	Calculation	Deviation (%)
1	1.70	1.74	1.70	2.30
3	–	2.14	2.08	2.88
5	2.39	2.50	2.45	1.97
7	–	2.84	2.83	0.35

gray curve in the sampling area. Because of the limited sampling area, a few random white spots significantly interfered with the grayscale curve, which in turn affected the resolution analysis results. Median filtering is sometimes used to eliminate noise in neutron radiography images. However, median filtering also leads to an overall decrease in imaging resolution, and the algorithm cannot eliminate white spots completely [31]. The theoretical resolution model does not consider the effect of electronic noise and background radiation, which is negligible compared with the radiation noise in a short imaging time. A quantitative study of the effect of radiation noise on image resolution is introduced in the next section.

4 Optimization of the theoretical resolution model for CTNR system

4.1 Correction of geometric distortion

The geometric distortion effect deviates from the projection position of the object, which leads to the horizontal stretching of the ESF curve. According to the above analysis, the total stretch length of the ESF curve is the sum of the spot position offsets D_g and D_s in Eqs. (3) and (4). The ESF after geometric distortion can be calculated using Eq. (6):

$$\mathrm{ESF_p} = \mathrm{ESF_0} + 0.8 \times \frac{d_c \cdot (t+d)}{L}, \tag{6}$$

where $\mathrm{ESF_p}$ denotes the actual resolution. $\mathrm{ESF_0}$ is the resolution at $d_c = 0$. The constant 0.8 is derived based on the ESF method (the difference value between 10% and 90%). Table 4 presents a comparison of the resolutions of the experimental, simulation, and theoretical results. These three results are in good agreement (deviation within 3%).

In the measurements, the MTF corresponding to a line pair was calculated using Eq. (1), and the input MTF (M_{in}) was fixed. Owing to geometric distortion, the gradient of the curve corresponding to the gray gradient of the line pair changed. However, this did not affect inputs I_{max} and I_{min} in the measurement of each line pair. The variety of MTF caused by the geometric distortion can be expressed as

$$\frac{\mathrm{MTF_p}}{\mathrm{MTF_0}} = \frac{I''_{max} - I''_{min}}{I'_{max} - I'_{min}}, \tag{7}$$

where $\mathrm{MTF_0}$ is the theoretical MTF, which is not affected by geometric distortion, and $\mathrm{MTF_p}$ is the MTF measured experimentally. The image of a slit was obtained by subtracting the ESF curves of the two edges of the slit. Because of the narrow width of the slit, the two curves are assumed to be identical. $I_{max} - I_{min}$ is proportional to the slope of the ESF curve. The slope is inversely proportional to the ESF resolution of the curve. According to Eq. (7), the measured $\mathrm{MTF_p}$ can be expressed as follows:

$$\frac{\mathrm{MTF_p}}{\mathrm{MTF_0}} = \frac{\mathrm{ESF_0}}{\mathrm{ESF_p}}, \tag{8}$$

where $\mathrm{ESF_p}$ denotes the ESF resolution of the line pair. $\mathrm{ESF_0}$ is the ESF resolution at $d_c = 0$. The relationship between $\mathrm{ESF_p}$ and $\mathrm{ESF_0}$ is obtained using Eq. (6). When the corresponding resolution of $\mathrm{ESF_0}$ and the theoretical resolution are assumed to be the same, the MTF at the line pair can be calculated as:

$$\mathrm{MTF_p} = \frac{\mathrm{MTF_0}}{1 + 0.8 \cdot \frac{d_c \cdot (t+d)}{L \cdot \mathrm{ESF_0}}}. \tag{9}$$

This equation was used to analyze the experimental data for calculating the MTF considering geometric distortion. The results were compared with those without correction and are shown in Table 5. After considering the influence of the geometric distortion, the maximum deviation was reduced from 23.1 to 8.82%. This indicates that geometric distortion is an important factor affecting the resolution of the CTNR system.

4.2 Correction of the radiation noise

The effect of radiation noise can be regarded as an independent factor, considering the irregularity in the scattering of fast neutrons. When the effect of noise is considered, the total MTF can be calculated as:

$$\begin{aligned} \mathrm{MTF_{ToT}}(u) = {} & \sin c\left(\frac{d}{L/D}u\right) \cdot \exp\left(-\pi(\delta u)^2\right) \\ & \cdot \sin c\left(\frac{\Delta s}{M_{CCD}}u\right) \cdot \mathrm{MTF_n}, \end{aligned} \tag{10}$$

where $\mathrm{MTF_{ToT}}$ is the total MTF value containing noise and $\mathrm{MTF_n}$ is the MTF of the noise.

This was because the noise distribution was random. Equation 1 can be used to derive $\mathrm{MTF_n}$. Within a fixed imaging area, the number of samplings included in the area is n,

Table 5 Comparison of resolutions between experiment and the correction model considering geometric distortion

L/D	Resolution of traditional model (mm)	Resolution of experiment (mm)	Deviation between experiment and traditional model (%)	Resolution of correction model considering geometric distortion (mm)	Deviation between experiment and correction model (%)
6.6	1.77	1.89	6.35	1.81	4.41
7.4	1.51	1.73	12.72	1.61	7.45
8.8	1.27	1.48	14.19	1.36	8.82
10	1.11	1.28	13.28	1.23	4.06
12	0.91	1.12	18.75	1.03	8.04

the proportion of noise in the image is σ, and the average gray value of noise is g. When noise is randomly added to the image, the increase in the gray value of each column is σng. Hence, $I'_{\max} = I_{\max} + \sigma ng$ and $I'_{\min} = I_{\min} + \sigma ng$. The $\mathrm{MTF_n}$ calculation formula is expressed as:

$$\mathrm{MTF_n} = \frac{M_{\mathrm{out}}}{M_{\mathrm{in}}} = \frac{\left[\left(I_{\max} + \sigma ng\right) - \left(I_{\min} + \sigma ng\right)\right] / \left[\left(I_{\max} + \sigma ng\right) + \left(I_{\min} + \sigma ng\right)\right]}{\left(I_{\max} - I_{\min}\right)/\left(I_{\max} + I_{\min}\right)} = \frac{1}{1 + 2\sigma ng/\left(I_{\max} + I_{\min}\right)}. \tag{11}$$

The gray value of the noise in an image is constant in a certain neutron radiography system. For single imaging, $I_{\max}$ and $I_{\min}$ are regarded as constants. Therefore, $ng/(I_{\max}+I_{\min})$ in Eq. (5) can be replaced by the constant r. Equation (11) can be simplified as:

$$\mathrm{MTF_n} = \frac{1}{1 + 2\sigma r}. \tag{12}$$

Equation (12) shows that the proportion of noise directly affects the modulation of the image. The MTF was negatively correlated with the proportion of noise. Experimental verification of Eq. (12) has been performed in detail in the literature [32].

In this study, white spot noise parameters were extracted from the experimental images to correct the theoretical calculation results. First, the white spot noise was recognized according to the abnormal gray gradient from the experimental image in Fig. 4. The average gray noise values and proportion of noise were calculated for each image. Subsequently, $\mathrm{MTF_n}$ for each image was calculated using Eq. (12). Table 6 lists the corrected theoretical and experimental results. After considering both the effects of geometric distortion and radiation noise, the maximum deviation between the theoretical model and the original experimental results was reduced to 4.22%. A small systematic deviation between the revised theoretical model and the experimental values was still observed. This is mainly due to the interference of non-fixed device factors, such as neutron scattering by the experimental sample.

5 Conclusion

A significant deviation in the resolution between the experiment and the traditional theoretical resolution model was observed in a neutron radiography experiment performed by HFIPS. To explain this phenomenon, the effects of a low L/D ratio and high-energy neutrons on imaging resolution were analyzed using Monte Carlo simulations. The results indicated that the deviation was primarily caused by geometric distortion and radiation noise. Additionally, through theoretical model optimization, the resolution deviation was effectively reduced by considering the imaging position and

Table 6 Comparison of resolutions between experiment and corrected model considering geometric distortion and radiation noise

L/D	Resolution of traditional model (mm)	Resolution of experiment (mm)	MTF_n	Resolution of correction model considering geometric distortion and radiation noise (mm)	Deviation between experiment and correction model (%)
6.6	1.77	1.89	0.851	1.86	1.07
7.4	1.51	1.73	0.805	1.67	3.59
8.8	1.27	1.48	0.813	1.42	4.22
10	1.11	1.28	0.909	1.24	3.13
12	0.91	1.12	0.791	1.09	2.75%

introducing a noise factor. The following conclusions were drawn.

(1) When the imaging position is far from the imaging center, geometric distortion leads to the degradation of image resolution in the CTNR system. The geometric distortion becomes significant with a decrease in *L*/*D*.
(2) The optical diffusion response of the converter screen was not independent of *L*/*D* under low *L*/*D* conditions. However, a change in δ has little effect on the resolution in a thin converter screen.
(3) The effect of nonthermal neutrons on the spatial resolution can be neglected in the CTNR system. However, the radiation noise induced by high-energy neutrons and secondary γ-rays will lead to a resolution degradation.
(4) Considering the effects of geometric distortion and radiation noise, the modified theoretical model agreed well with the experimental results. The maximum deviation decreased from 23.1 to 4.22%.

This study analyzed the factors affecting imaging resolution in a low *L*/*D* environment, which is the main difference between the CTNR system and a traditional TNR system. Currently, resolution degradation caused by geometric distortion and radiation noise has not been fundamentally solved. The design improvement of the moderating collimator and performance optimization of imaging systems are key directions for future research.

Author contributions All authors contributed to the study conception and design. Material preparation, data collection and analysis were performed by Lian-Xin Zhang, Si-Ze Chen and Zao-Di Zhang. The first draft of the manuscript was written by Lian-Xin Zhang and all authors commented on previous versions of the manuscript. All authors read and approved the final manuscript.

Data availability The data that support the findings of this study are openly available in Science Data Bank at https://www.doi.org/10.57760/sciencedb.j00186.00071 and http://resolve.pid21.cn/31253.11.sciencedb.j00186.00071.

Conflict of interest The authors declare that they have no competing interests.

References

1. M.W. Johnson, The industrial uses of neutrons. Appl. Radiat. Isot. **46**(6–7), 673–680 (1995)
2. Y.P. Cheng, R. Han, Z.W. Li et al., Imaging internal density structure of the Laoheishan volcanic cone with cosmic ray muon radiography. Nucl. Sci. Tech. **33**(7), 88 (2022). https://doi.org/10.1007/s41365-022-01072-4
3. F.C. De Beer, M. Coetzer, D. Fendeis et al., Neutron radiography and other NDE tests of main rotor helicopter blades. Appl. Radiat. Isotopes. **61**(4), 609–616 (2004). https://doi.org/10.1016/j.apradiso.2004.03.088
4. J.G. Fantidis, The use of electron linac for high quality thermal neutron radiography unit. Nucl. Instrum. Meth. A. **908**, 361–366 (2018). https://doi.org/10.1016/j.nima.2018.08.114
5. P. Hardt, H. Röttger, Neutron radiography handbook: nuclear science and technology. Springer Sci. Bus. Med. **21**, 1–30 (2012)
6. Z.Y. Guo, Y. Zou, Y. Lu et al., Neutron radiography with compact accelerator at Peking University: problems and solutions. Physcs. Proc. **26**, 70–78 (2012). https://doi.org/10.1016/j.phpro.2012.03.011
7. S.R. Malkawi, N. Ahmad, Prediction and measurement of neutron energy spectrum in a material test research reactor. Ann. Nucl. Energy. **27**(4), 311–327 (2000). https://doi.org/10.1016/s0306-4549(99)00057-2
8. D.P. Kozlenko, S.E. Kichanov, E.V. Lukin et al., Neutron radiography facility at IBR-2 high flux pulsed reactor: first results. Physcs. Proc. **69**, 87–91 (2015). https://doi.org/10.1016/j.phpro.2015.07.012
9. K.M. Nazarov, B. Muhametuly, E.A. Kenzhin et al., New neutron radiography and tomography facility TITAN at the WWR-K reactor. Nucl. Instrum. Meth. A. **982**, 164572 (2020). https://doi.org/10.1016/j.nima.2020.164572
10. K.K. Mishra, A.I. Hawari, V.H. Gillette, Design and performance of a thermal neutron imaging facility at the North Carolina State University PULSTAR reactor. IEEE Trans. Nucl. Sci. **53**(6), 3904–3911 (2006). https://doi.org/10.1109/tns.2006.884323
11. Y. Kiyanagi, Neutron imaging at compact accelerator-driven neutron sources in Japan. J. Imag. **4**(4), 55 (2018). https://doi.org/10.3390/jimaging4040055
12. S. Bishnoi, P.S. Sarkar, R.G. Thomas et al., Preliminary experimentation of fast neutron radiography with DT neutron generator at BARC. J. Nondestruct. Eval. **38**(1), 1–9 (2019). https://doi.org/10.1007/s10921-018-0550-9
13. Z.Y. Guo, Y. Lu, Y. Zou et al., Progress of PKUNIFTY–a RFQ accelerator based neutron imaging facility at Peking University. Physcs. Proc. **43**, 79–85 (2013). https://doi.org/10.1016/j.phpro.2013.03.010
14. S. Wang, W. Bin, B. Liu et al., A moveable neutron imaging facility using DT neutron source based on a compact accelerator. Appl. Radiat. Isotopes. **169**, 109564 (2021). https://doi.org/10.1016/j.apradiso.2020
15. H.Z. Bilheux, R. McGreevy, I.S. Anderson (ed.), Neutron imaging and applications (2009). https://doi.org/10.1007/978-0-387-78693-3
16. Y. Wang, S.B. Han, L.F. He et al., Calculation methods for neutron radiography spatial resolution. Nucl. Tech. **354**, 275–280 (2012). https://doi.org/10.11889/j.0253-3219.2014.hjs.37.040502. (**in Chinese**)
17. L.F. He, S.B. Han, Y. Wang et al., Calculation and analysis of the neutron radiography spatial resolution. Nucl. Tech. **37**, 040502 (2014). https://doi.org/10.11889/j.0253-3219.2014.hjs.37.040502. (**in Chinese**)
18. S. Agostinelli, J. Allison, K. Amako et al., GEANT4—a simulation toolkit. Nucl. Instrum. Meth. A. **506**, 250–303 (2003). https://doi.org/10.1016/s0168-9002(03)01368-8
19. J. Allison, K. Amako, J. Apostolakis et al., Recent developments in Geant4. Nucl. Instrum. Meth. A. **835**, 186–225 (2016). https://doi.org/10.1016/j.nima.2016.06.125
20. Y. Lu, Z. Xu, L.X. Zhang et al., GEANT4 simulations of the neutron beam characteristics for 9be/7li targets bombarded by the low energy protons. Nucl. Instrum. Meth. B. **506**, 8–14 (2021). https://doi.org/10.1016/j.nimb.2021.09.005

21. A. Datta, A.I. Hawari, Geant4 analysis of a thermal neutron real-time imaging system. IEEE. T. Nucl. Sci. **64**(7), 1652–1658 (2017). https://doi.org/10.1109/tns.2017.2708031
22. J. Guo, T. Bucherl, Y. Zou et al., Comparison of the performance of different converters for neutron radiography and tomography using fission neutrons. Nucl. Instrum. Meth. A. **605**, 69–72 (2009). https://doi.org/10.1016/j.nima.2009.01.129
23. S.Y. Luo, Y.H. Huang, X.T. Ji et al., Hybrid model for muon tomography and quantitative analysis of image quality. Nucl. Sci. Tech. **33**(7), 81 (2022). https://doi.org/10.1007/s41365-022-01070-6
24. A.A. Harms, B.K. Garside, P.S.W. Chan et al., Edge-spread function in neutron radiography. J. Appl. Phys. **43**(9), 3863–3867 (1972). https://doi.org/10.1063/1.1661825
25. S. Steven, *Digital Signal Processing: A Practical Guide for Engineers and Scientists* (Elsevier, Amsterdam, 2013)
26. E. Gronenschild, Correction for geometric image distortion in the x-ray imaging chain: Local technique versus global technique. Med. Phys. **26**(12), 2602–2616 (1999). https://doi.org/10.1118/1.598800
27. J. Qin, J.Y. Ni, L.F. Ye et al., Thin-film approximate point scattered function and its application to neutron radiography. Nucl. Sci. Tech. **33**(9), 109 (2022). https://doi.org/10.1007/s41365-022-01094-y
28. A. Khorshidi, H. Ghafoori-Fard, M. Sadeghi, Epithermal neutron formation for boron neutron capture therapy by adiabatic resonance crossing concept. Int. J. Mod. Phys. E. **23**(05), 1450032 (2014). https://doi.org/10.1142/s0218301314500323
29. A. Khorshidi, M. Sadeghi, A. Pazirandeh et al., Radioanalytical prediction of radiative capture in 99Mo production via transmutation adiabatic resonance crossing by cyclotron. J. Radioanal. Nucl. Ch. **299**(1), 303–310 (2014). https://doi.org/10.1007/s10967-013-2749-7
30. F. James, F. Ziegler, J.P. Biersack et al., SRIM, the stopping and range of ions in matter. Nucl. Instrum. Meth. B. **268**, 1818–1823 (2008). https://doi.org/10.1016/j.nimb.2010.02.091
31. X.N. Cao, Z.D. Zhang, S.Z. Chen et al., Application of improved self-adaptive weighted median filtering algorithm in neutron radiography, in 2021 6th International Conference on Intelligent Computing and Signal Processing (ICSP). IEEE, pp. 50–55 (2021). https://doi.org/10.1109/icsp51882.2021.9408883
32. J. Yu, S.Z. Chen, L.X. Zhang et al., Influence of CCD camera transient noise on imaging resolution and shielding requirement in neutron radiography. Atomic Energy Sci. Technol. **55**, 7 (2021). https://doi.org/10.7538/yzk.2020.youxian.0855 (in Chinese)